

HiPoNet: A Topology-Preserving Multi-View Neural Network For High Dimensional Point Cloud and Single-Cell Data

Siddharth Viswanath*¹ Hiren Madhu*¹ Dhananjay Bhaskar^{1,2} Jake Kovalic³ Dave Johnson⁴ Rex Ying¹
 Christopher Tape⁵ Ian Adelstein⁶ Michael Perlmutter^{4,7} Smita Krishnaswamy^{1,2,8,9,10}

Abstract

In this paper, we propose HiPoNet, an end-to-end differentiable neural network for regression, classification, and representation learning on high-dimensional point clouds. Single-cell data can have high dimensionality exceeding the capabilities of existing methods for point clouds which are tailored for 3D data. Moreover, modern single-cell and spatial experiments now yield entire cohorts of datasets (i.e. one on every patient), necessitating models that can process large, high-dimensional point clouds at scale. Most current approaches build a single nearest-neighbor graph, discarding important geometric information. In contrast, HiPoNet forms higher-order simplicial complexes through learnable feature reweighting, generating multiple data views that disentangle distinct biological processes. It then employs simplicial wavelet transforms to extract multi-scale features—capturing both local and global topology. We empirically show that these components preserve topological information in the learned representations, and that HiPoNet significantly outperforms state-of-the-art point-cloud and graph-based models on single cell. We also show an application of HiPoNet on spatial transcriptomics datasets using spatial co-ordinates as one of the views. Overall, HiPoNet offers a robust and scalable solution for high-dimensional data

*Equal contribution ¹Department of Computer Science, Yale University, New Haven, USA ²Department of Genetics, Yale University, New Haven, USA ³Department of Applied Physics, Yale University, New Haven, USA ⁴Program in Computing, Boise State University, Idaho, USA ⁵Cell Communication Lab, Department of Oncology, University College London Cancer Institute, London, UK ⁶Department of Mathematics, Yale University, New Haven, USA ⁷Department of Mathematics, Boise State University, Idaho, USA ⁸Computational Biology and Bioinformatics Program, Yale University, New Haven, USA ⁹Wu-Tsai Institute, Yale University, New Haven, USA ¹⁰Program for Applied Math, Yale University, New Haven, USA. Correspondence to: Smita Krishnaswamy <krishnaswamy.smita@yale.edu>.

Preprint. Under review.

analysis.

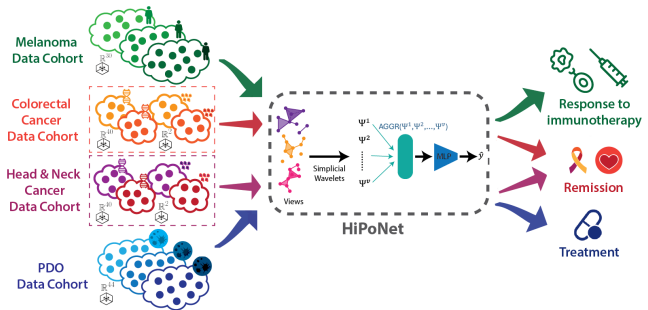


Figure 1. The HiPoNet pipeline.

1. Introduction

High dimensional point clouds, i.e., sets of points $\mathcal{X} = \{\mathbf{x}_i\}_{i=1}^n \subseteq \mathbb{R}^d$ now arise in many fields—most prominently single cell analysis (Venkat et al., 2023; Ramos Zapatero et al., 2023; Chew et al., 2022; MacDonald et al., 2023; Ahlmann-Eltze & Huber, 2025; Kröger et al., 2024), where using modern technologies such as mass cytometry or scRNA-seq, large cohorts of patients can now be measured producing several high dimensional data matrices. Further, technologies like perturb-seq enable the possibility of studying single-cell data under many conditions leading to comparable cohorts of datasets. Thus machine learning techniques that once reasoned about data points and classified data points, now have to reason about entire datasets. This serves as the motivation for HiPoNet illustrated in Figure 1.

Generally, single cell analysis methods like UMAP (McInnes et al., 2020) or PHATE (Moon et al., 2019) reduce point clouds defined by single-cell data into an individual graph learned from all features (often in the tens of thousands). However, this single graph may not specifically organize cells according to processes defined by subsets of dimensions. For instance, cells may be in a specific phase of the cell cycle which would be revealed by an organization based on cell cycle genes, or at

a certain point in a differentiation process which would be revealed by stem cell genes. On the other hand, existing neural network methods for point cloud data, such as PointNet (Qi et al., 2017a) and its variants (Qi et al., 2017b; Zhao et al., 2021; Wang et al., 2019; Ma et al., 2022) are primarily designed for 3D point clouds and rely on spatially localized features¹. Hence they are not able to handle high-dimensional point clouds or disentangle processes from high dimensional data. As a result, there is a growing need to develop a neural network that can efficiently handle these diverse high-dimensional point clouds, ingest them seamlessly, encode the cellular processes, and perform various downstream machine learning tasks on them. To address these limitations, we introduce **HiPoNet**.

In HiPoNet, rather than using one view of the cells as represented by a single graph, we introduce the idea of multiple views, each of which is learned using a feature reweighting vector, thus potentially detangling and making implicit biological processes explicit. Further, rather than modeling the data as a graph we model it as a simplicial complex that captures higher-order relationships between cells, which HiPoNet analyzes using multiscale wavelets. Overall, we gain a rich representation that disentangles processes by capturing hierarchical relationships and separating overlapping biological processes, while preserving geometric and topological information of the underlying point clouds. Preserving the structure is important because it reflects the intrinsic geometry and topology of the data, providing a better interpretation of complex biological processes, and hence improving downstream analysis.

To capture global structure using a neural network, we use a wavelet-based multiscale message aggregation scheme rather than traditional message passing in graph and simplicial neural networks, which struggle to capture long-range dependencies and multiscale relationships. Although newer models like graph transformers (Dwivedi & Bresson, 2020) can capture long range dependencies, they are also limited in terms of expressive power. When applied on these point clouds, they only work on a single graph and are unable to preserve the intrinsic geometric structure of the graph. However, using diffusion wavelets defined on simplicial complexes, we show theoretically that 1) we capture the underlying geometry of the point cloud, 2) we capture the 0-homology (connected components) of the underlying cloud, 3) we capture curvature of the point cloud. Empirically we show that we can predict persistence homology directly from our simplicial neural network, without explicitly computing topological signatures or reducing the data to those features. These properties that are preserved by HiPoNet are essential for projecting the pointcloud into subspaces that may drive a particular classification, such as response

to immunotherapy, or drug treatment response.

The key features of HiPoNet include:

- **Learning multiple views the the data:** We introduce a learnable scaling mechanism to reweight each feature in a high dimensional feature vector, which we then use to learn a graph to organize data by the processes represented by the particular view.
- **Higher order constructions:** We learn simplicial complexes by conducting a VR filtration of the data, downstream neural networks built on this complex retain geometric and topological information including volume, curvature, connected components and holes in the data. We also offer the option of learning graphs from these views for cases that have high computational complexity.
- **Multiscale Message Passing:** Rather than simple message aggregation schemes that smooth data, we use multiscale simplicial wavelets to aggregate features over the simplicial complex. This can find crucial groupings of data to inform final classification, from local to global without oversmoothing.

We showcase the utility of HiPoNet using three state-of-the-art single cell *data cohorts* which we have curated. Note we use the term data cohort to refer to ensembles of single-cell data sets, collected on many patients or under many conditions. The first data cohort includes melanoma patients undergoing immune checkpoint blockade immunotherapy, where the task is to classify the patient response based on multiplex ion beam imaging (MIBI) datasets of T-cells, with protein expression features. Each patient here has between 489 to 1784 cells. The second data cohort features multiple patient-derived-(cancer) organoids (PDOs) from each of 12 different patients with colorectal cancer. In these PDOs, cancer cells are taken from each patient and grown as multiple 3D organoids with and without other cell types as well as in the presence of several treatments. Here, we test the ability of the neural network to uncover the treatments applied to each PDO based on the ensemble cellular states. Each organoid in this dataset has approximately 1137 cells. The final cohort features Spatial Transcriptomics data from about 500 human cancer biopsies from head-and-neck and colorectal cancer patients, capturing 40 distinct protein markers. This is an immunofluorescent imaging dataset, which is capable of measuring dozens of protein markers in a single tissue sample while preserving the spatial arrangement of cells, offering rich insights into the tumor microenvironments through spatial and gene expression view. This technology of collecting spatial data and protein markers is called spatial transcriptomics, and it is an emerging technology playing a pivotal role in advanced cancer research. These datasets highlight the scalability and diversity

¹We discuss these techniques more in Section A .

of HiPoNet in handling complex, high dimensional biological point cloud data.

2. Background

A simplicial complex \mathcal{S} (Schaub et al., 2018; Barbarossa & Sardellitti, 2020) is defined as a finite collection of simplices that satisfies the principle of inclusion. A k -simplex, denoted as σ_k , is a non-empty subset of \mathcal{X} containing $k + 1$ points. For any $\sigma_k \in \mathcal{S}$, all non-empty subsets of σ_k must also belong to \mathcal{S} . If τ_{k-1} is a subset of σ_k that contains k points, we say that τ_{k-1} is a face of σ_k . The order of a simplicial complex, K , is determined by the highest-order simplex contained within \mathcal{S} , so therefore a simplicial complex \mathcal{S} contains simplices of orders $k = 0, 1, \dots, K$. Note that when $K = 1$, a simplicial complex is essentially equivalent to an unweighted, undirected graph, where the 0-simplices and 1-simplices are the vertices and edges. Features of simplices across all orders are denoted as $\mathbf{X} = \{\mathbf{X}_0, \mathbf{X}_1, \dots, \mathbf{X}_K\}$, where $\mathbf{X}_k \in \mathbb{R}^{N_k \times D_k}$, where D_k is the feature dimension of k -simplices.

In a simplicial complex \mathcal{S} , a k -simplex $\sigma_k \in \mathcal{S}$ can have four types of neighbors:

- **Boundary adjacent neighbors or faces:** These are the $(k - 1)$ -simplices τ_{k-1} that are faces of σ_k , denoted as $\mathcal{N}_{\mathcal{B}}(\sigma_k) = \{\tau_{k-1} : \tau_{k-1} \subset \sigma_k\}$.
- **Coboundary adjacent neighbors or co-faces:** These are all $(k + 1)$ -simplices τ_{k+1} which have σ_k as a face, denoted as $\mathcal{N}_{\mathcal{C}}(\sigma_k) = \{\tau_{k+1} : \sigma_k \subset \tau_{k+1}\}$.
- **Lower adjacent neighbors:** These are simplices τ_k of the same order as σ_k that share a common face, ρ_{k-1} , represented as $\mathcal{N}_{\mathcal{L}}(\sigma_k) = \{\tau_k : \rho_{k-1} = \sigma_k \cap \tau_k, |\rho_{k-1}| = k - 1\}$.
- **Upper adjacent neighbors:** These are simplices, τ_k of the same order as σ_k that are contained in a common $(k + 1)$ -simplex $\rho_{k+1} \in \mathcal{S}$, given by $\mathcal{N}_{\mathcal{U}}(\sigma_k) = \{\tau_k : \rho_{k+1} = \sigma_k \cup \tau_k, |\rho_{k+1}| = k + 1\}$.

The 1-hop neighborhood of a simplex σ_k is given by $\mathcal{N}_1(\sigma_k) = \cup\{\sigma_k, \mathcal{N}_{\mathcal{B}}(\sigma_k), \mathcal{N}_{\mathcal{C}}(\sigma_k), \mathcal{N}_{\mathcal{L}}(\sigma_k), \mathcal{N}_{\mathcal{U}}(\sigma_k)\}$. While, the m -hop neighborhood of a simplex σ_k is defined recursively as $\mathcal{N}_m(\sigma_k) = \cup_{\tau \in \mathcal{N}_{m-1}(\sigma_k)} \mathcal{N}_1(\tau)$ for $m \geq 2$.

The relationships between k -simplices and their faces are encoded in the boundary matrix of order k , denoted as $\mathbf{B}_k \in \mathbb{R}^{N_{k-1} \times N_k}$, where N_k is the number of simplices of order k contained in \mathcal{S} . The (i, j) -th entry of \mathbf{B}_k is defined to be equal to 1 if the i -th $(k - 1)$ -simplex is a face of the j -th k -simplex and is defined to be zero otherwise. We note that these boundary matrices are defined in terms of only boundary adjacent and co-boundary adjacent neighbors. However, they may also be used to construct the following

Laplacian matrices which encode information about lower adjacent and upper adjacent neighbors.

- **Lower Laplacian:** The lower adjacent neighbors of k -simplices are represented by $\mathbf{L}_k^l = \mathbf{B}_k^\top \mathbf{B}_k$.
- **Upper Laplacian:** The upper adjacent neighbors of k -simplices are represented by $\mathbf{L}_k^u = \mathbf{B}_{k+1} \mathbf{B}_{k+1}^\top$.

These Laplacian matrices, along with the boundary matrices, provide a comprehensive representation of the structure and relationships within a simplicial complex, making them valuable tools for modeling and analyzing complex data.

2.1. Simplicial Random Walks

Simplicial random walks extend the concept of traditional random walks from graphs to simplicial complexes, enabling a richer representation of the data which is able to encode higher-order features. Unlike standard graph-based random walks, which model transitions between nodes (vertices), simplicial random walks capture transitions between k -simplices (e.g., points, edges, triangles, tetrahedra), thereby incorporate higher-order interactions.

The diffusion process in simplicial complexes is governed by the k -Hodge Laplacian, which encodes both lower and upper adjacency relationships:

$$\Delta_k = \mathbf{L}_k^l + \mathbf{L}_k^u, \quad (1)$$

where \mathbf{L}_k^l and \mathbf{L}_k^u represent the lower and upper Laplacians, respectively. The simplicial random walk is represented by the transition matrix \mathbf{P}_k , which describes the probability of transitioning between k -simplices within the complex. It is defined as:

$$\mathbf{P}_k = \Delta_k \mathbf{D}_k^{-1}, \quad (2)$$

where $\mathbf{D}_k = \text{diag}(\Delta_k \mathbf{1})$ is a diagonal matrix that normalizes the transition probabilities, ensuring that \mathbf{P}_k is a valid stochastic matrix, i.e., that its columns sum to one. With the transition matrix \mathbf{P}_k , a walker walks from a k -simplex σ_k to another k -simplex τ_k with probability $\mathbf{P}_{k, \sigma_k, \tau_k}$.

By modeling transitions at the level of simplices rather than just nodes, simplicial random walks provide a more expressive framework for understanding diffusion and connectivity in complex topological spaces.

2.2. Heat Diffusion on Simplicial Complexes

The heat equation on simplicial complexes (Hua & Luo, 2017) generalizes the classical notion of heat diffusion on graphs (or other domains) to higher-dimensional structures. The heat equation on k -simplices is then given by:

$$\frac{\partial u_k(\sigma_k, t)}{\partial t} = -\Delta_k u_k(\sigma_k, t) \quad (3)$$

where $u_k(\sigma_k, t)$ represents the heat at simplex σ_k at time t . To solve this equation, an initial condition must be specified. For each k -simplex $\sigma_k = \{\mathbf{x}_{\sigma_k^0}, \mathbf{x}_{\sigma_k^1}, \dots, \mathbf{x}_{\sigma_k^k}\}$, the initial condition is constructed from the node features of its constituent vertices. Specifically, if $\mathbf{h}_0(\mathbf{x}_{\sigma_k^i})$ denotes the features of vertex $\mathbf{x}_{\sigma_k^i}$, where $\mathbf{h}_0(\cdot)$ is a transformation function, then the initial condition for the simplex σ_k is given by:

$$u_k(\sigma_k, 0) = f(\mathbf{h}_0(\mathbf{x}_{\sigma_k^0}), \mathbf{h}_0(\mathbf{x}_{\sigma_k^1}), \dots, \mathbf{h}_0(\mathbf{x}_{\sigma_k^k})), \quad (4)$$

where f is a function that aggregates the node features of the vertices in σ_k . Common choices for f include the mean, sum, or other symmetric functions of the node features.

The heat equation is widely used to model diffusive phenomena. In this higher-order generalization, it describes how an initial distribution of heat propagates over the simplicial complex over time. The k -Laplacian ensures that the diffusion process respects the higher-order connectivity of the complex, encoding both its topological and geometric structure.

3. Methodology

In this section, we describe the proposed method HiPoNet, a high-dimensional point cloud neural network designed to learn expressive representations of an input point set $\mathcal{X} = \{\mathbf{x}_1, \mathbf{x}_2, \dots, \mathbf{x}_n\} \in \mathbb{R}^d$. As summarized in Algorithm 1, our framework comprises three primary steps:

1. **Learnable Feature Weighting:** We learn a set of weights $\alpha^{(v)}$ to highlight the most informative dimensions, yielding reweighted point clouds $\tilde{\mathcal{X}}^{(v)}$.
2. **Multi-view Learning:** From each $\tilde{\mathcal{X}}^{(v)}$, we construct a higher-order Vietoris-rips complex $\mathcal{S}^{(v)}$ (Vietoris, 1927). This approach allows us to capture not only pairwise relationships but also higher-order interactions within the data, preserving richer topological and *volume* features. This process is repeated K times, generating multiple views of the original point cloud to capture the underlying geometry of the point cloud.
3. **Multi-scale Feature Extraction:** For each simplicial complex $\mathcal{S}^{(v)}$, we apply the wavelet transform according to the structure, to produce multi-scale embeddings $\Psi^{(v)}$, capturing both local and global relationships. These embeddings are then concatenated into a single representation Φ , which is passed to a multilayer perceptron (MLP) to yield the final predictions $\hat{\mathbf{y}}$.

By combining learnable feature weighting, multiview simplicial complex construction, and wavelet transforms, HiPoNet leverages multiple perspectives of the underlying manifold to deliver robust, scalable representations for high-dimensional point clouds.

Algorithm 1 HiPoNet

Input : Point cloud \mathcal{X} , kernel bandwidth σ , number of views V .

Learnable Parameters: learnable weights $\alpha^{(v)}$, and MLP \mathbf{z} .

Output : Predictions $\hat{\mathbf{y}}$.

```

1 for  $v \leftarrow 1$  to  $V$  do
2    $\tilde{\mathbf{x}}_i^{(v)} = \alpha^{(v)} \odot \mathbf{x}_i$  where  $\odot$  is Hadamard product, i.e.,
   element-wise multiplication, and  $i \in \{1, \dots, n\}$ ;
3    $\tilde{\mathcal{X}}^{(v)} = \{\tilde{\mathbf{x}}_i^{(v)} : i \in \{1, \dots, n\}\}$ ;
4    $\mathcal{S}^{(v)} = \text{Vietoris-Rips}(\tilde{\mathcal{X}}^{(v)}, \epsilon)$ ;
5    $\tilde{\mathbf{B}}^{(v)}, \tilde{\mathbf{X}}^{(v)} = \text{CalculateBX}(\mathcal{S}^{(v)})$ ;
6   Calculate the multiscale features  $\Psi(\tilde{\mathbf{B}}^{(v)}, \tilde{\mathbf{X}}^{(v)})$ ;
7  $\Phi = \text{Aggr}\{\Psi(\tilde{\mathbf{B}}^{(1)}, \tilde{\mathbf{X}}^{(1)}), \Psi(\tilde{\mathbf{B}}^{(2)}, \tilde{\mathbf{X}}^{(2)}), \dots, \Psi(\tilde{\mathbf{B}}^{(V)}, \tilde{\mathbf{X}}^{(V)})\}$ ;
8  $\hat{\mathbf{y}} = \mathbf{z}(\Phi)$ 
9 return  $\hat{\mathbf{y}}$ .
```

3.1. Point Cloud Feature learning

In many real-world scenarios, such as scRNA-seq, feature vectors can encode critical properties, such as gene expression levels. However, not all dimensions (or genes) contribute equally to a downstream task, and irrelevant or noisy features can impair model performance, especially in high-dimensional settings.

To address this, we introduce a learnable weighting mechanism that dynamically adjusts the importance of each feature dimension. Concretely, we define V distinct weight vectors $\alpha^{(v)}$, $1 \leq v \leq V$, each as a parameter of the model. For the v -th view, each point \mathbf{x}_i is rescaled to

$$\tilde{\mathbf{x}}_i^{(v)} = \alpha^{(v)} \odot \mathbf{x}_i = [\alpha_1^{(v)} x_{i1}, \alpha_2^{(v)} x_{i2}, \dots, \alpha_d^{(v)} x_{id}],$$

where \odot denotes the Hadamard (elementwise) product. We stack all reweighed points to create the reweighed point cloud $\tilde{\mathcal{X}}^{(v)} = \{\tilde{\mathbf{x}}_1^{(v)}, \tilde{\mathbf{x}}_2^{(v)}, \dots, \tilde{\mathbf{x}}_n^{(v)}\}$. The operation of reweighing point clouds amplifies more informative dimensions for the task at hand while downplaying less relevant features, effectively relieving the need for manual feature engineering. In the context of single-cell data, where the feature space can be vast, such automated reweighing is crucial for isolating key gene expressions that drive improved downstream performance. The learned weights can also be used for other biological insights, such as which gene markers are important for cancer diagnosis.

3.2. Multi-View Learning

Next, for each reweighed set $\tilde{\mathcal{X}}^{(v)}$, we create a simplicial complex $\mathcal{S}^{(v)}$. We define kernelized distances between two

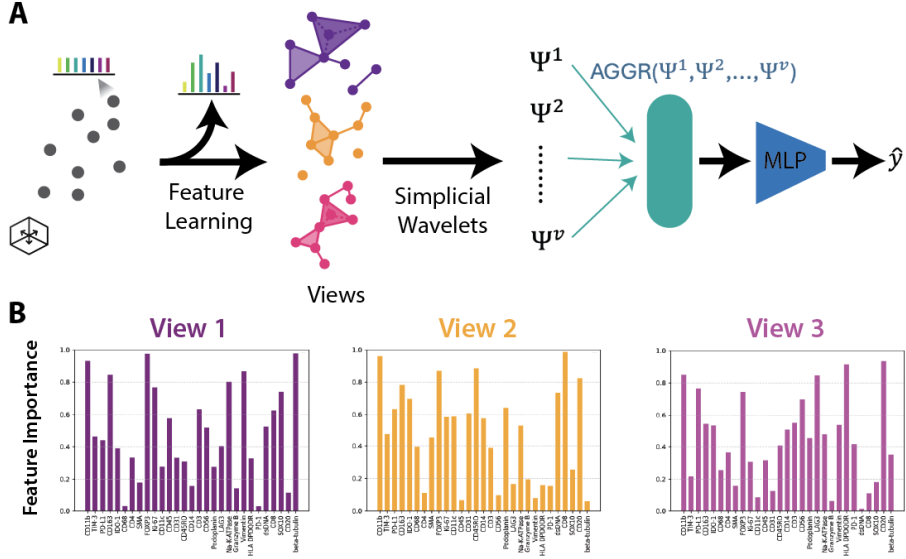


Figure 2. (A) The HiPoNet architecture. (B) Feature importance visualized across three learned views

points $\tilde{\mathbf{x}}_i^{(v)}$ and $\tilde{\mathbf{x}}_j^{(v)}$ as:

$$d_{i,j}^{(v)} = \exp\left(\frac{\|\tilde{\mathbf{x}}_i^{(v)} - \tilde{\mathbf{x}}_j^{(v)}\|_2^2}{2\sigma^2}\right).$$

We then fix a scale parameter, ϵ and construct the Vietoris-Rips Complex $\mathcal{S}^{(v)}$, a simplicial complex defined by the rule that $\sigma_k = \{\tilde{\mathbf{x}}_{i_0}^{(v)}, \tilde{\mathbf{x}}_{i_1}^{(v)}, \dots, \tilde{\mathbf{x}}_{i_k}^{(v)}\}$ is an element of $\mathcal{S}^{(v)}$ if $d_{i_p, i_q}^{(v)} \leq \epsilon$ for all $1 \leq p, q \leq k$. The kernelized distance metric is important as it emphasizes local similarities making it more robust to noise. After constructing the simplicial complex $\mathcal{S}^{(v)}$, we construct the boundary operators $\tilde{\mathbf{B}}^{(v)}$ and feature matrices $\tilde{\mathbf{X}}^{(v)}$. We use a custom implementation of the Vietoris-rips filtration that enables us to make simplicial construction differentiable, making HiPoNet end-to-end trainable.

We repeat this process V times, and construct $\tilde{\mathbf{B}}^{(v)}$ for each view $1 \leq v \leq V$. By constructing an ensemble of simplicial complexes $\mathcal{S}^{(1)}, \mathcal{S}^{(2)}, \dots, \mathcal{S}^{(V)}$, our method integrates V distinct perspectives of the original high-dimensional point cloud. Constructing a simplicial complex $\mathcal{S}^{(v)}$ for each reweighted set $\tilde{\mathcal{X}}^{(v)}$ allows the model to disentangle and analyze distinct subspaces or biological processes captured by each view. Each complex focuses on a different cellular process, capturing unique local and global structures that is overlooked when relying on a single representation. Consequently, subsequent learning stages benefit from a richer set of structural cues, enhancing the overall representation quality for downstream tasks.

3.3. Multi-scale feature extraction

After the simplicial complexes have been constructed, we can leverage geometric deep learning methods to compute representations for the point cloud. Although message passing neural networks (MPNNs) for simplicial complexes (Battiloro et al., 2024; Bodnar et al., 2021; Giusti et al., 2022) have been introduced, they often suffer from oversmoothing effects (Balcilar et al., 2021), where representations become indistinguishable after multiple layers. In addition, oversquashing (Alon & Yahav, 2021) is another constraint of such message-passing frameworks. As the receptive field of each node grows, large amounts of information from distant nodes are compressed or ‘‘squashed’’ into a fixed-size vector, leading to loss of important information between the nodes. This limits the ability of MPNNs to model long-range dependencies. Furthermore, MPNNs require large amounts of data to train and calculate expressive representations (Madhu et al., 2024), which hinders their ability to learn expressive representations for the data. These limitations lead to suboptimal performance, as capturing the long-term information is crucial to understanding the topology of the data, enhancing representation quality, and improving downstream task performance.

In order to address these shortcomings, we employ the simplicial wavelet transform (Madhu et al., 2024) (SWT). The SWT $\Psi(\Delta, \mathbf{X})$ is a multi-scale feature extractor for processing a signal \mathbf{X} defined on the simplices represented by \mathbf{B} . These wavelets are based on diffusion wavelets introduced in (Coifman & Maggioni, 2006) which utilize random walk matrices at different time scales. In SWT, the random walk matrices are calculated first as per Eq 2. Then, features are iteratively aggregated over all the neighborhoods and stored

for each scale j . Finally, a difference between different scales is taken to extract multiscale features. These steps are described in detail below.

Diffusion: In the simplicial wavelet transform (SWT), diffusion plays a crucial role in capturing multi-scale structural information within a simplicial complex. The diffusion process governs how information propagates across simplices of different orders over time. For view v , diffusion is guided by the random walk matrix $\mathbf{P}_k^{(v)}$ calculated using the k -Hodge Laplacian $\Delta_k^{(v)}$ as per Eq 2, which encodes both lower and upper adjacencies of simplices, ensuring that diffusion respects the higher-order topology of the complex. The signals are propagated using powers of the diffusion operator as $\mathbf{X}_k^{(v)(j)} = \mathbf{P}_k^{(v)j} \mathbf{X}_k^{(v)}$ where $\mathbf{X}_k^{(v)}$ represents the initial feature matrix of k -simplices, and $\mathbf{X}_k^{(v)(j)}$ captures the transformed features after j iterations of diffusion.

Definition 3.1 (Simplicial Wavelet Transform). The simplicial wavelet transform at scale j is defined as the difference between transformed signals at consecutive scales:

$$\Psi_k^{(v)(j)} = \mathbf{X}_k^{(v)(j)} - \mathbf{X}_k^{(v)(j-1)}, \quad (5)$$

where $\mathbf{X}_k^{(j)}$ is the feature representation at scale j . This difference operator acts as a high-pass filter, highlighting high-frequency components of the signal, which correspond to variations in the structure of the simplicial complex.

After applying SWT for multiple scales j and all orders k , we apply a non-linearity, which we choose to be the absolute value $|\cdot|$, inspired from [Bruna & Mallat \(2012\)](#). The features are then aggregated over all the scales as:

$$\Psi_k^{(v)} = \bigcup_{i=1}^J \{|\Psi_k^{(v)(1)}|, |\Psi_k^{(v)(2)}|, \dots, |\Psi_k^{(v)(j)}|\};$$

The final feature set of is denoted as:

$$\Psi(\tilde{\Delta}^{(v)}, \tilde{\mathbf{X}}^{(v)}) = \{\Psi_0^{(v)}, \Psi_1^{(v)}, \dots, \Psi_K^{(v)}\};$$

After extracting features for each view v , we aggregate the features over views as:

$$\Phi = \text{Aggr}\{\Psi(\tilde{\mathbf{B}}^{(1)}, \tilde{\mathbf{X}}^{(1)}), \Psi(\tilde{\mathbf{B}}^{(2)}, \tilde{\mathbf{X}}^{(2)}), \dots, \Psi(\tilde{\mathbf{B}}^{(V)}, \tilde{\mathbf{X}}^{(V)})\}.$$

3.4. Training

Once the multiscale features Φ are extracted from the set of graphs, we process these features through a multilayer perceptron (MLP) \mathbf{z} to generate predictions for the target downstream task. Formally, the predictions are computed as:

$$\hat{\mathbf{y}} = \mathbf{z}(\Phi),$$

where Φ represents the concatenated multi-scale embeddings derived from the graph wavelet transforms, and $\hat{\mathbf{y}}$

denotes the predicted labels or outputs depending on the task (e.g., classification, regression, etc.).

To optimize the model parameters, we employ the cross-entropy loss function, which is particularly effective for classification tasks. This setup ensures that the extracted multi-scale features are effectively utilized, improving the overall performance on downstream tasks.

4. Theoretical results

In this section, provide theoretical motivation for our model. Specifically, we first show that heat diffusion on simplices captures the 0-homology of the point cloud. Then, we show that simplicial complexes can be expanded into a graph, and the heat equation on the simplicial complex agrees with the heat equation on the equivalent graph. Then, we show that the diffusion operators can capture geodesic distances.

4.1. Heat Diffusion and Connectivity

A simplicial complex is said to be connected if any two simplices can be linked by a sequence of simplices that share common faces. More formally, for any two simplices σ and τ , there exists $m \geq 0$ such that $\tau \in \mathcal{N}_m(\sigma)$. If a simplicial complex is not connected, it can be decomposed into a union of disjoint connected components, each of which is a maximal connected subcomplex.

The following theorem demonstrates that the solution to the heat equation on a simplicial complex remains confined to the connected components where the initial condition is supported. This reflects the intuitive idea that heat cannot diffuse across disconnected regions of the complex. This proposition also aligns with the concept of 0-homology in algebraic topology. Thus, the connected components of a simplicial complex correspond to the generators of its 0-homology group. The heat equation’s confinement to connected components ensures that diffusion dynamics respect the 0-homology structure of the simplicial complex.

Theorem 4.1. *The heat equation, Eq 3, respect the 0-homology structure of the simplicial complex.*

The proof of Theorem 4.1 is available in Appendix B. The heat equation on a simplicial complex is governed by the Hodge-Laplacian Δ_k , which acts locally by coupling only simplices are neighbors. If the initial condition is confined to a subset of simplices, the locality of Δ_k ensures that heat diffusion cannot propagate beyond the connected components containing this subset. Consequently, the solution to the heat equation respects the 0-homology structure of the simplicial complex, preserving the disjointness of connected components.

4.2. Heat Diffusion on Simplicial Graphs

In this section, we demonstrate that the solution to the heat equation on a simplicial complex \mathcal{S} agrees with the solution to the heat equation on an associated simplicial graph $\mathcal{G}(\mathcal{S})$. The simplicial graph is a higher-dimensional generalization of a graph, where vertices represent simplices of all orders, and edges encode adjacency and boundary relationships. This construction allows us to compare heat diffusion on the simplicial complex with heat diffusion on a graph-like structure, providing a simplified yet equivalent framework for analysis. Additionally, single-cell datasets lie on an underlying Riemannian manifold.

Definition 4.2 (Simplicial Graph). Let \mathcal{S} be a simplicial complex of order K , and let Σ_k denote the set of k -simplices in \mathcal{S} for $k = 0, 1, \dots, K$. The simplicial graph $\mathcal{G}(\mathcal{S})$ associated with \mathcal{S} is a graph defined as follows:

1. The vertex set $V(\mathcal{G})$ is the union of all simplices in \mathcal{S} :

$$V(\mathcal{G}) = \bigcup_{k=0}^K \Sigma_k$$
2. The edge set $E(\mathcal{G})$ consists of pairs of simplices that are adjacent or share a boundary relationship: $E(\mathcal{G}) = \{\{\sigma, \sigma'\} \mid \sigma, \sigma' \in V(\mathcal{G}), \sigma' \in \mathcal{N}_1(\sigma), \sigma \neq \sigma'\}$

Proposition 4.3. *The heat equation on simplicial complex \mathcal{S} agrees with the heat equation on the associated simplicial graph $\mathcal{G}(\mathcal{S})$.*

The proof of Proposition 4.3 is available in Appendix C. The diffusion operator $\Delta_{\mathcal{G}}$ on the simplicial graph can be represented by placing the Hodge Laplacians in a block diagonal fashion. Similarly, heat value vectors for each order can be stacked to create a single vector. By doing so, the heat equation on the simplicial graph $\frac{\partial u_{\mathcal{G}}(\cdot, t)}{\partial t}$ can be represented by a combination of heat equations on the k -simplices $\frac{\partial u_k(\cdot, t)}{\partial t}$ for all $k \in \{0, \dots, K\}$.

4.3. Heat Solution Captures Geometry

In this section, we establish that the diffusion operator on the simplicial complex can approximate geodesic distances and other geometric quantities on the underlying manifold. This result demonstrates a theoretical link between diffusion processes and the geometry of the data manifold. Of course there are many representations of the data as a manifold, and implicit in the following is the application of the manifold assumption to the simplicial graph $\mathcal{G}(\mathcal{S})$ representation of the data.

Theorem 4.4. *Assume that a transformed point cloud $\tilde{\mathcal{X}}^{(v)}$ lies upon a Riemannian manifold \mathcal{M} . Then, the diffusion operators Δ_k on the associated simplicial complexes can approximate geodesic distances on the underlying manifold.*

Given the equivalence between the heat kernel on \mathcal{S} and $\mathcal{G}(\mathcal{S})$, and the discrete nature of \mathcal{G} , we can define a heat

kernel on the simplicial graph. Then, the result follows directly from Varadhan’s formula (Varadhan, 1967), which states that for any closed Riemannian manifold (M, g) , the geodesic distance $d(x, y)$ can be approximated using the heat kernel $H_t(\sigma, \tau)$ (Huguet et al., 2023).

The proof of Theorem 4.4 is available in Appendix D. This theorem formalizes the link between diffusion processes, as captured by the heat equation, and the geometric structure of the data manifold. This connection allows us to extract meaningful geometric information from the heat kernel. Furthermore, computation of geodesic distances on manifolds is computationally expensive and often infeasible in high dimensions. By using diffusion-based approximations, we can efficiently estimate geodesic distances with discrete operators on simplicial graphs. Furthermore, the equivalence between diffusion and geodesic distances provides a theoretical basis for manifold learning methods, enabling tasks such as dimensionality reduction, clustering, and visualization on high-dimensional data.

There is a long literature (starting with (Coifman & Maggioni, 2006)) relating the Laplacian and the diffusion operator to the geometry of the data manifold. There is subsequent work that measures the curvature of the data manifold via the diffusion operator (Bhaskar et al., 2022). More relevant to the exposition in this section are the results which relate the asymptotic expansion of the trace of the heat kernel to geometric quantities like dimension, volume, and total scalar curvature (see for instance (Mihai, 2006)). Indeed, following immediately from Proposition 4.3 we have:

Corollary 4.5. *The equivalence between the heat kernel on \mathcal{S} and $\mathcal{G}(\mathcal{S})$ implies the equivalence of dimension, volume, and total scalar curvature on the respective underlying data manifolds.*

Proof. The eigenvalues λ_i and corresponding eigenfunctions ϕ_i of the Laplace-Beltrami operator determine the heat kernel via the spectral expansion:

$$K(t, x, y) = \sum_{i=0}^{\infty} e^{-\lambda_i t} \phi_i(x) \phi_i(y)$$

The eigenvalues are influenced by the volume and curvature of the manifold via Weyl’s law (Weyl, 1911) and the eigenvalue comparison theorems (Cheng, 1975). \square

5. Empirical Results

We compare the performance of HiPoNet with KNN-GNNs as well as PointNet++ and its variants described in Section F.1. The KNN-based graph neural networks (GCN (Kipf & Welling, 2017), SAGE (Hamilton et al., 2017), GAT (Velickovic et al., 2018), GIN (Xu et al., 2019)

Model	Melanoma	PDO
KNN-GCN	72.72 ± 5.45	53.66 ± 0.70
KNN-SAGE	76.36 ± 6.03	55.89 ± 0.83
KNN-GAT	61.81 ± 4.45	52.56 ± 10.06
KNN-GIN	<u>85.45 ± 3.63</u>	<u>57.02 ± 1.20</u>
KNN-GraphTransformer	80.00 ± 8.90	39.46 ± 2.78
DGCNN	63.33 ± 12.47	40.00 ± 4.36
PointNet++	45.00 ± 22.42	45.24 ± 2.08
PointTransformer	79.99 ± 6.24	30.00 ± 4.70
HiPoNet	90.90 ± 4.92	63.10 ± 0.0

Table 1. Accuracies on classification tasks.

and Graph Transformer (Dwivedi & Bresson, 2020)) are presented in the first block, followed by point cloud oriented models (DGCNN (Wang et al., 2019), PointNet++ (Qi et al., 2017b), PointTransformer (Zhao et al., 2021)), and finally the proposed HiPoNet. A bolded score indicates the highest overall performance, whereas an underlined value identifies the second-best performance. We present the mean and standard deviation over 5 seeds². The hyperparameters are described in Section F.

5.1. Topology and Geometry Prediction

We evaluate HiPoNet on the task of predicting persistence features of the point clouds, which provides a topological summary of the dataset. The ground truth for persistence diagram prediction were created on the datasets described in Appendix E. The purpose of this task is to show that HiPoNet’s representation contains this information, but downstream tasks may use more information than just the topological signature or curvature.

The results in Table 3 indicate that HiPoNet consistently outperforms all baseline methods, achieving the lowest MSE across all datasets. Notably, KNN-based models perform competitively, with KNN-SAGE and KNN-GIN showing relatively lower errors compared to other GNN-based approaches. However, point-cloud-based models (DGCNN, PointNet++, and PointTransformer) exhibit significantly higher error values, suggesting that they struggle to capture the necessary topological features for persistence feature prediction. Overall, the superior performance of HiPoNet demonstrates its ability to effectively learn and predict topological structures from high-dimensional point clouds, making it a robust choice for persistence feature analysis in biological datasets.

5.2. Single Cell data classification

Next we assess the performance of HiPoNet on single-cell data cohorts which we have curated (as shown in Table 2). Detailed descriptions of the biological data is described in the Appendix E. However, each data cohort is a measurement of thousands cells on a large cohort of patients and the

²The code is available at <https://github.com/KrishnaswamyLab/PointCloudNet>.

label is prediction of outcome (of disease or treatment).

Data cohort	Avg. Points/Dataset	Total # Datasets	Task	Data Modality
Melanoma patient samples	1137	54	Response to Immunotherapy	MIBI
Patient-derived organoids (PDOs)	3273	1625	Treatment Administered	Mass Cytometry
Charville	1000	196	Outcome to chemotherapy	
	1000	196	Cancer recurrence	
UPMC	1000	308	Outcome to chemotherapy	CODEX
	1000	308	Cancer recurrence	
DFCI	1000	54	Outcome to chemotherapy	

Table 2. Information about single-cell data

For classification task, as we can see in Table 1, HiPoNet consistently achieves the top results on all four datasets, demonstrating a robust ability to handle high-dimensional inputs such as single-cell data. KNN-GIN generally fares best among the KNN-based models but experiences a notable accuracy gap compared to some point cloud methods on Melanoma. Meanwhile, PointNet++ and PointTransformer perform relatively inconsistently across different tasks.

In Table 6, we present an ablation study examining how the number of views used in HiPoNet. While adding more views can yield better performance by capturing increasingly rich multi-view information, it results in diminishing returns after a point. In Table 6 (see Appendix) we conduct an ablation study on the number of views, and see that our best results are achieved when we use four views to capture the topology of the point clouds.

5.3. Application to spatial transcriptomics data

In addition to the experiments on single-cell data, we further demonstrate an application of HiPoNet in analyzing spatial transcriptomics data. Unlike previous experiments where multiple learned views were used, here we construct two distinct views: one capturing spatial proximity of cells and the other encoding gene expression similarity. Table 4 compares the predictive performance of various models on spatial transcriptomics data drawn from three different cohorts: DFCI, Charville, and UPMC. Each cohort includes two tasks—either outcome prediction or recurrence prediction—resulting in five total evaluations. Notably, HiPoNet achieves the top results in most settings, outperforming both KNN-based graph neural networks (GCN, SAGE, GAT, GIN) and PointNet++.

6. Conclusion

In this work, we introduce a novel neural network for high-dimensional point cloud datasets by leveraging multiple-views, higher-order constructs, and multi-scale wavelet transforms. We show that HiPoNet learns different views from each dataset, preserves geometric and topological structures, and improves downstream analysis across diverse single-cell and spatial transcriptomics data cohorts by overcoming the limitations of state-of-the-art point cloud and graph-based models.

Model	Melanoma	PDO
KNN-GCN	1.0683 ± 0.002	1.0454 ± 0.018
KNN-SAGE	0.734 ± 0.031	1.0338 ± 0.010
KNN-GAT	1.101 ± 0.028	1.068 ± 0.008
KNN-GIN	0.850 ± 0.061	1.2605 ± 0.006
KNN-GraphTransformer	1.274 ± 0.038	1.3754 ± 0.006
DGCNN	28.412 ± 0.001	1353.0262 ± 1.12
PointNet++	28.418 ± 0.001	28.417 ± 0.005
PointTransformer	28.422 ± 0.014	28.41 ± 0.003
HiPoNet	0.633 ± 0.043	0.4046 ± 0.006

Table 3. MSE on prediction of persistence features.

Data Task	Charville			UPMC	
	DCCI Outcome	Outcome	Recurrence	Outcome	Recurrence
KNN-GCN	0.597 ± 0.049	0.547 ± 0.010	0.642 ± 0.056	0.668 ± 0.032	0.5 ± 0.0
KNN-SAGE	0.82 ± 0.040	0.618 ± 0.021	0.581 ± 0.016	0.631 ± 0.013	0.5 ± 0.0
KNN-GAT	0.557 ± 0.047	0.675 ± 0.051	0.530 ± 0.032	0.647 ± 0.029	0.5 ± 0.0
KNN-GIN	0.700 ± 0.048	0.609 ± 0.020	0.624 ± 0.045	0.663 ± 0.015	0.514 ± 0.02
KNN-GraphTransformer	0.668 ± 0.051	0.578 ± 0.040	0.5 ± 0.0	0.6290 ± 0.008	0.5 ± 0.0
PointNet++	0.491 ± 0.057	0.451 ± 0.078	0.499 ± 0.001	0.506 ± 0.01	0.495 ± 0.00
HiPoNet	0.916 ± 0.03	0.681 ± 0.012	0.681 ± 0.01	0.665 ± 0.01	0.6044 ± 0.0

Table 4. AUC ROC on Spatial Transcriptomics Classification

Acknowledgments

D.B. received funding from the Yale - Boehringer Ingelheim Biomedical Data Science Fellowship and the Kavli Institute for Neuroscience Postdoctoral Fellowship. M.P. acknowledges funding from The National Science Foundation under grant number OIA-2242769. S.K. is funded in part by the NIH (NIGMSR01GM135929, R01GM130847), NSF CAREER award IIS- 2047856, NSF DMS grant 2327211 and NSF CISE grant 2403317. S.K. and M.P. also acknowledge funding from NSF-DMS Grant No. 2327211.

Impact Statement

This work aims to accelerate cancer research, immunotherapy development, and precision medicine by providing a scalable, biologically informed, and robust neural network for high-dimensional point clouds.

References

Ahlmann-Eltze, C. and Huber, W. Analysis of multi-condition single-cell data with latent embedding multivariate regression. *Nature Genetics*, Jan 2025. ISSN 1546-1718. doi: 10.1038/s41588-024-01996-0. URL <https://doi.org/10.1038/s41588-024-01996-0>.

Alon, U. and Yahav, E. On the bottleneck of graph neural networks and its practical implications. In *International Conference on Learning Representations*, 2021. URL <https://openreview.net/forum?id=i800PhOCVH2>.

Angelo, M., Bendall, S. C., Finck, R., Hale, M. B., Hitzman, C., Borowsky, A. D., Levenson, R. M., Lowe, J. B., Liu, S. D., Zhao, S., et al. Multiplexed ion beam imaging of human breast tumors. *Nature medicine*, 20(4):436–442, 2014.

Balcilar, M., Renton, G., Héroux, P., Gaüzère, B., Adam, S., and Honeine, P. Analyzing the expressive power of graph neural networks in a spectral perspective. In *International Conference on Learning Representations*, 2021. URL <https://openreview.net/forum?id=-qh0M9XWxnv>.

Barbarossa, S. and Sardellitti, S. Topological signal processing over simplicial complexes. *IEEE Transactions on Signal Processing*, 68:2992–3007, 2020. ISSN 1941-0476. doi: 10.1109/tsp.2020.2981920. URL <http://dx.doi.org/10.1109/TSP.2020.2981920>.

Battiloro, C., Testa, L., Giusti, L., Sardellitti, S., Lorenzo, P. D., and Barbarossa, S. Generalized simplicial attention neural networks, 2024. URL <https://arxiv.org/abs/2309.02138>.

Bhaskar, D., MacDonald, K., Fasina, O., Thomas, D., Rieck, B., Adelstein, I., and Krishnaswamy, S. Diffusion curvature for estimating local curvature in high dimensional data, 2022. URL <https://arxiv.org/abs/2206.03977>.

Bodnar, C., Frasca, F., Wang, Y. G., Otter, N., Montúfar, G., Liò, P., and Bronstein, M. M. Weisfeiler and leman go topological: Message passing simplicial networks. *CoRR*, abs/2103.03212, 2021. URL <https://arxiv.org/abs/2103.03212>.

Bruna, J. and Mallat, S. Invariant scattering convolution networks. *CoRR*, abs/1203.1513, 2012. URL <http://arxiv.org/abs/1203.1513>.

Cheng, S.-Y. Eigenvalue comparison theorems and its geometric applications. *Mathematische Zeitschrift*, 1975. URL <https://doi.org/10.1007/BF01214381>.

Chew, J., Steach, H., Viswanath, S., Wu, H.-T., Hirn, M., Needell, D., Vesely, M. D., Krishnaswamy, S., and Perlmutter, M. The manifold scattering transform for high-dimensional point cloud data. In Cloninger, A., Doster, T., Emerson, T., Kaul, M., Ktena, I., Kvinge, H., Miolane, N., Rieck, B., Tymochko, S., and Wolf, G. (eds.), *Proceedings of Topological, Algebraic, and Geometric Learning Workshops 2022*, volume 196 of *Proceedings of Machine Learning Research*, pp. 67–78. PMLR, 25 Feb–22 Jul 2022. URL <https://proceedings.mlr.press/v196/chew22a.html>.

Coifman, R. and Maggioni, M. Diffusion wavelets. *Appl. Comp. Harm. Anal.*, 21(1):53–94, 2006.

Dwivedi, V. P. and Bresson, X. A generalization of transformer networks to graphs. *CoRR*, abs/2012.09699, 2020. URL <https://arxiv.org/abs/2012.09699>.

- Giusti, L., Battiloro, C., Lorenzo, P. D., Sardellitti, S., and Barbarossa, S. Simplicial attention neural networks, 2022. URL <https://arxiv.org/abs/2203.07485>.
- Hamilton, W., Ying, Z., and Leskovec, J. Inductive representation learning on large graphs. In *Advances in Neural Information Processing Systems (NeurIPS)*, pp. 1024–1034, 2017. URL <https://arxiv.org/abs/1706.02216>.
- Hua, B. and Luo, X. Davies-gaffney-grigor’yan lemma on simplicial complexes, 2017. URL <https://arxiv.org/abs/1702.00529>.
- Huguet, G., Tong, A., Brouwer, E. D., Zhang, Y., Wolf, G., Adelstein, I., and Krishnaswamy, S. A heat diffusion perspective on geodesic preserving dimensionality reduction. In *Thirty-seventh Conference on Neural Information Processing Systems*, 2023. URL <https://openreview.net/forum?id=HNd4qTJxkW>.
- Kipf, T. N. and Welling, M. Semi-supervised classification with graph convolutional networks. In *International Conference on Learning Representations (ICLR)*, 2017. URL <https://arxiv.org/abs/1609.02907>.
- Kröger, C., Müller, S., Leidner, J., Kröber, T., Warnat-Herresthal, S., Spintge, J. B., Zajac, T., Neubauer, A., Frolov, A., Carraro, C., Freiesleben, S. D., Altenstein, S., Rauchmann, B., Kilimann, I., Coenjaerts, M., Spottke, A., Peters, O., Priller, J., Perneckzy, R., Teipel, S., Düzel, E., Jessen, F., Puccio, S., Aschenbrenner, A. C., Schultze, J. L., Pecht, T., Beyer, M. D., Bonaguro, L., and Group, D. S. Unveiling the power of high-dimensional cytometry data with cycondor. *Nature Communications*, 15(1):10702, Dec 2024. ISSN 2041-1723. doi: 10.1038/s41467-024-55179-w. URL <https://doi.org/10.1038/s41467-024-55179-w>.
- Loshchilov, I. and Hutter, F. Fixing weight decay regularization in adam. *CoRR*, abs/1711.05101, 2017. URL <http://arxiv.org/abs/1711.05101>.
- Ma, X., Qin, C., You, H., Ran, H., and Fu, Y. Rethinking network design and local geometry in point cloud: A simple residual mlp framework, 2022. URL <https://arxiv.org/abs/2202.07123>.
- MacDonald, K., Bhaskar, D., Thampakkul, G., Nguyen, N., Zhang, J., Perlmutter, M., Adelstein, I., and Krishnaswamy, S. A flow artist for high-dimensional cellular data, 2023. URL <https://arxiv.org/abs/2308.00176>.
- Madhu, H., Gurugubelli, S., and Chepuri, S. P. Unsupervised parameter-free simplicial representation learning with scattering transforms. In Salakhutdinov, R., Kolter, Z., Heller, K., Weller, A., Oliver, N., Scarlett, J., and Berkenkamp, F. (eds.), *Proceedings of the 41st International Conference on Machine Learning*, volume 235 of *Proceedings of Machine Learning Research*, pp. 34145–34160. PMLR, 21–27 Jul 2024. URL <https://proceedings.mlr.press/v235/madhu24a.html>.
- McInnes, L., Healy, J., and Melville, J. Umap: Uniform manifold approximation and projection for dimension reduction, 2020. URL <https://arxiv.org/abs/1802.03426>.
- Mihai, I. Chapter 6 complex differential geometry. volume 2 of *Handbook of Differential Geometry*, pp. 383–435. North-Holland, 2006. doi: [https://doi.org/10.1016/S1874-5741\(06\)80009-9](https://doi.org/10.1016/S1874-5741(06)80009-9). URL <https://www.sciencedirect.com/science/article/pii/S1874574106800099>.
- Moon, K. R., Van Dijk, D., Wang, Z., Gigante, S., Burkhardt, D. B., Chen, W. S., Yim, K., Elzen, A. v. d., Hirn, M. J., Coifman, R. R., et al. Visualizing structure and transitions in high-dimensional biological data. *Nature biotechnology*, 37(12):1482–1492, 2019.
- Ptacek, J., Vesely, M., Rimm, D., Hav, M., Aksoy, M., Crow, A., and Finn, J. 52 characterization of the tumor microenvironment in melanoma using multiplexed ion beam imaging (mibi). *Journal for ImmunoTherapy of Cancer*, 9(Suppl 2):A59–A59, 2021. doi: 10.1136/jitc-2021-SITC2021.052. URL https://jitc.bmj.com/content/9/Suppl_2/A59.
- Qi, C. R., Su, H., Mo, K., and Guibas, L. J. Pointnet: Deep learning on point sets for 3d classification and segmentation, 2017a. URL <https://arxiv.org/abs/1612.00593>.
- Qi, C. R., Yi, L., Su, H., and Guibas, L. J. Pointnet++: Deep hierarchical feature learning on point sets in a metric space. *CoRR*, abs/1706.02413, 2017b. URL <http://arxiv.org/abs/1706.02413>.
- Ramos Zapatero, M., Tong, A., Opzooomer, J. W., O’Sullivan, R., Cardoso Rodriguez, F., Sufi, J., Vlckova, P., Nattress, C., Qin, X., Claus, J., Hochhauser, D., Krishnaswamy, S., and Tape, C. J. Trellis tree-based analysis reveals stromal regulation of patient-derived organoid drug responses. *Cell*, 186(25):5606–5619.e24, 2023. ISSN 0092-8674. doi: <https://doi.org/10.1016/j.cell.2023.11.005>. URL <https://www.sciencedirect.com/science/article/pii/S0092867423012205>.
- Schaub, M. T., Benson, A. R., Horn, P., Lippner, G., and Jadbabaie, A. Random walks on simplicial complexes and the normalized hodge laplacian. *CoRR*,

- abs/1807.05044, 2018. URL <http://arxiv.org/abs/1807.05044>.
- van der Maaten, L. and Hinton, G. Visualizing data using t-sne. *Journal of Machine Learning Research*, 9(86):2579–2605, 2008. URL <http://jmlr.org/papers/v9/vandermaaten08a.html>.
- Varadhan, S. R. S. On the behavior of the fundamental solution of the heat equation with variable coefficients. *Communications on Pure and Applied Mathematics*, 20(2):431–455, 1967. doi: <https://doi.org/10.1002/cpa.3160200210>. URL <https://onlinelibrary.wiley.com/doi/abs/10.1002/cpa.3160200210>.
- Velickovic, P., Cucurull, G., Casanova, A., Romero, A., Lio, P., and Bengio, Y. Graph attention networks. In *International Conference on Learning Representations (ICLR)*, 2018. URL <https://arxiv.org/abs/1710.10903>.
- Venkat, A., Bhaskar, D., and Krishnaswamy, S. Multiscale geometric and topological analyses for characterizing and predicting immune responses from single cell data. *Trends in Immunology*, 44(7):551–563, 2023. ISSN 1471-4906. doi: <https://doi.org/10.1016/j.it.2023.05.003>. URL <https://www.sciencedirect.com/science/article/pii/S1471490623000844>. Special issue: Systems immunology II.
- Vesely, M. and Johnson, D. Processed multiplexed ion beam imaging (mibi) of tumor microenvironments of 54 melanoma samples following immunotherapy, 2025. URL <https://data.mendeley.com/datasets/79y7bht7tf/1>.
- Vietoris, L. Über den höheren zusammenhang kompakter räume und eine klasse von zusammenhangstreuen abbildungen. *Mathematische Annalen*, 1927. URL <https://doi.org/10.1007/BF01447877>.
- Wang, Y., Sun, Y., Liu, Z., Sarma, S. E., Bronstein, M. M., and Solomon, J. M. Dynamic graph cnn for learning on point clouds, 2019. URL <https://arxiv.org/abs/1801.07829>.
- Weyl, H. Nachrichten von der gesellschaft der wissenschaften zu göttingen. *Mathematisch-Physikalische Klasse*, 1911.
- Wu, Z., Trevino, A. E., Wu, E., Swanson, K., Kim, H. J., D’Angio, H. B., Preska, R., Charville, G. W., Dalerba, P. D., Egloff, A. M., Uppaluri, R., Duvvuri, U., Mayer, A. T., and Zou, J. Space-gm: geometric deep learning of disease-associated microenvironments from multiplex spatial protein profiles. *bioRxiv*, 2022. doi: 10.1101/2022.05.12.491707. URL <https://www.biorxiv.org/content/early/2022/05/13/2022.05.12.491707>.
- Xu, K., Hu, W., Leskovec, J., and Jegelka, S. How powerful are graph neural networks? In *International Conference on Learning Representations (ICLR)*, 2019. URL <https://arxiv.org/abs/1810.00826>.
- Yeo, Y. Y., Cramer, P., Deisher, A., Bai, Y., Zhu, B., Yeo, W.-J., Shipp, M. A., Rodig, S. J., and Jiang, S. A hitchhiker’s guide to high-dimensional tissue imaging with multiplexed ion beam imaging. *Methods in cell biology*, 186:213, 2024.
- Zhao, H., Jiang, L., Jia, J., Torr, P., and Koltun, V. Point transformer, 2021. URL <https://arxiv.org/abs/2012.09164>.

A. Related Works

The vast majority of work on point cloud-based learning has focused on three dimensional problems, such as mapping and interpreting sensor readings in computer vision or localization tasks (Qi et al., 2017a;b; Zhao et al., 2021; Ma et al., 2022; Wang et al., 2019). Early methods such as PointNet (Qi et al., 2017a) and its successor PointNet++ (Qi et al., 2017b) introduced permutation-invariant models with the ability to extract local and global features from 3D point clouds. Newer methods such as Dynamic Graph Convolutional Neural Network (DGCNN) (Wang et al., 2019) leverage dynamic graph representations to better extract rich features from input point clouds, while PointMLP (Ma et al., 2022) and Point Transformer (Zhao et al., 2021) use standard Multilayer Perceptrons and local self-attention mechanism as the building blocks for better performance in classification and regression tasks. Previous methods provide motivation for our line of inquiry, but since the biological domains in which we are interested frequently have orders of magnitude more dimensions ranging from dozens in proteomics datasets to thousands in transcriptomic datasets, we require a new approach that is not limited by architectural decisions and is computationally efficient when working with high-dimensional data. Despite the advancements in these existing methods, they are fundamentally designed for 3D point clouds and struggle with performance and scalability in a high dimensional setting as they rely on spatial heuristics, because local neighborhoods become less meaningful in high-dimension. As opposed to this, HiPoNet is able to scale to high-dimensional data while also preserving the geometry of the dataset.

Single-cell analysis has greatly benefited from graph-based methods that learns global structure from high-dimensional data. These methods typically rely on a *single* graph construct to infer relationships between cellular states. Methods such as UMAP (McInnes et al., 2020) and t-SNE (van der Maaten & Hinton, 2008) perform non-linear dimensionality reduction by constructing a neighborhood graph and embedding cells into a low-dimensional space. On the other hand, PHATE (Moon et al., 2019) is a dimensionality reduction method that captures both global and local nonlinear structure but only constructs a *single* graph from the data. While these methods have been useful in understanding various biological processes, they may fail to organize cells based on processes governed by subsets of dimensions with just a single connectivity structure. In contrast to this, HiPoNet has the ability to model distinct cellular processes by leveraging its multi-view framework, preserving important geometric properties.

B. Proof of Theorem 4.1

Proposition B.1 (Connected Components on Simplicial Complexes). *Let S be a simplicial complex of order K with m connected components, and let Σ_k the set of k -simplices ($k \leq K$). We partition $\Sigma_k = \Sigma_{k,1} \sqcup \Sigma_{k,2} \sqcup \dots \sqcup \Sigma_{k,m}$, where each $\Sigma_{k,i}$ corresponds to the k -simplices in a single connected component. Let S be a subset of n -simplices, defined as the union of several connected components: $S = \Sigma_{n,i_1} \sqcup \dots \sqcup \Sigma_{n,i_k}$. Assume the initial condition $\mathbf{x} = u(\cdot, 0)$ of the diffusion equation has support contained in S . Then, for any simplex $\sigma \notin S$ of order k and for all $t > 0$, we have:*

$$u_k(\sigma, t) = 0. \tag{6}$$

Proof. The Hodge-Laplacian Δ_k acts locally, meaning it only couples simplices that share common faces. As a result, if the initial condition $u(\cdot, 0)$ has support contained in S , the solution $u(\sigma, t)$ must remain confined to S for all $t > 0$. To formalize this, define a function $\tilde{u}(\sigma, t)$ as follows:

$$\tilde{u}_k(\sigma, t) = \begin{cases} u_k(\sigma, t), & \text{if } \sigma \in S, \\ 0, & \text{if } \sigma \notin S. \end{cases}$$

We will show that $\tilde{u}_k(\sigma, t)$ satisfies the same heat equation as $u(\sigma, t)$.

First, consider a simplex $\sigma \in S$. By definition, $\tilde{u}_k(\sigma, t) = u(\sigma, t)$, and since $u_k(\sigma, t)$ satisfies the heat equation, it follows that:

$$\frac{\partial \tilde{u}(\sigma, t)}{\partial t} = -\Delta_k \tilde{u}_k(\sigma, t).$$

Next, consider a simplex $\sigma \notin S$. By definition, $\tilde{u}_k(\sigma, t) = 0$ for all $t \geq 0$ and $\frac{\partial \tilde{u}_k(\sigma, t)}{\partial t} = 0$. Since Δ_k only couples simplices within the same connected component, and σ is not in S , we have: $\Delta_k \tilde{u}_k(\sigma, t) = 0$. Thus, $\tilde{u}_k(\sigma, t)$ trivially satisfies the heat equation.

Since $\tilde{u}_k(\sigma, t)$ satisfies the heat equation for all simplices $\sigma \in \mathcal{S}$ and coincides with the initial condition $u(\cdot, 0)$ on \mathcal{S} , it follows from the uniqueness of solutions to the heat equation that $\tilde{u}_k(\sigma, t) = u_k(\sigma, t)$ for all $t > 0$. Therefore, for any simplex $\sigma \notin \mathcal{S}$ and for all $t > 0$, we have: $u_k(\sigma, t) = \tilde{u}_k(\sigma, t) = 0$. \square

C. Proof of Proposition 4.3

Proposition C.1 (Agreement of Heat Equation Solutions). *Let \mathcal{S} be a simplicial complex of order K , and let $\mathcal{G}(\mathcal{S})$ be its associated simplicial graph as defined in Definition 4.2. Let $u_{\mathcal{S}}(\sigma, t)$ denote the solution to the heat equation on \mathcal{S} (Eqn. 3). Similarly, let $u_{\mathcal{G}}(v, t)$ denote the solution to the heat equation on $\mathcal{G}(\mathcal{S})$:*

$$\frac{\partial u_{\mathcal{G}}(v, t)}{\partial t} = -\Delta_{\mathcal{G}} u_{\mathcal{G}}(v, t), \quad (7)$$

where $\Delta_{\mathcal{G}}$ is the graph Laplacian of $\mathcal{G}(\mathcal{S})$. Assuming that the initial conditions $u_{\mathcal{S}}(\cdot, 0)$ and $u_{\mathcal{G}}(\cdot, 0)$ are consistent, i.e.,

$$u_{\mathcal{S}}(\sigma, 0) = u_{\mathcal{G}}(\sigma, 0) \quad \text{for all } \sigma \in V(\mathcal{G}).$$

Then, for all $t > 0$ and for all simplices $\sigma \in \mathcal{S}$, the solutions agree: $u_{\mathcal{S}}(\sigma, t) = u_{\mathcal{G}}(\sigma, t)$.

The simplicial wavelet transform incorporates diffusion in multiple orders using the diffusion operator for each order. However, these diffusion operators can be represented using one large diffusion operator on the simplicial graph \mathcal{G} , resulting in the block-diagonal Laplacian $\Delta_{\mathcal{G}} \in \mathbb{R}^{N \times N}$:

$$\Delta_{\mathcal{G}} = \begin{bmatrix} \Delta_0 & \mathbf{0} & \mathbf{0} & \cdots & \mathbf{0} & \mathbf{0} \\ \mathbf{0} & \Delta_1 & \mathbf{0} & \cdots & \mathbf{0} & \mathbf{0} \\ \mathbf{0} & \mathbf{0} & \Delta_2 & \cdots & \mathbf{0} & \mathbf{0} \\ \vdots & \vdots & \vdots & \ddots & \vdots & \vdots \\ \mathbf{0} & \mathbf{0} & \mathbf{0} & \cdots & \Delta_{K-1} & \mathbf{0} \\ \mathbf{0} & \mathbf{0} & \mathbf{0} & \cdots & \mathbf{0} & \Delta_K \end{bmatrix} \quad (8)$$

where $N = \sum_{i=0}^K N_i$. Now, for each k -simplex σ_k , the function $u_k(\sigma_k, t)$ represents the heat value at σ_k at time t . Collectively, the vector

$$u_k(\cdot, t) = [u_k(\sigma_k^{(1)}, t), u_k(\sigma_k^{(2)}, t), \dots]^{\top}$$

stores these values for *all* k -simplices, in some fixed ordering. Since \mathcal{G} treats *all* simplices as nodes, a single node index v in \mathcal{G} could correspond to either a 0-simplex, a 1-simplex, and so on, up to a K -simplex. Hence, when we form a global vector by effectively stacking the heat vectors for each order as:

$$u_{\mathcal{G}}(v, t) = \begin{bmatrix} u_0(\cdot, t) \\ u_1(\cdot, t) \\ u_2(\cdot, t) \\ \vdots \\ u_K(\cdot, t) \end{bmatrix},$$

By stacking the diffusion operators and heat vectors in this manner, the heat equation on the simplicial graph becomes

$$\begin{aligned}
 \frac{\partial u_{\mathcal{G}}(\cdot, t)}{\partial t} &= -\Delta_{\mathcal{G}} u_{\mathcal{G}}(\cdot, t) \\
 &= \begin{bmatrix} \Delta_0 & \mathbf{0} & \mathbf{0} & \cdots & \mathbf{0} & \mathbf{0} \\ \mathbf{0} & \Delta_1 & \mathbf{0} & \cdots & \mathbf{0} & \mathbf{0} \\ \mathbf{0} & \mathbf{0} & \Delta_2 & \cdots & \mathbf{0} & \mathbf{0} \\ \vdots & \vdots & \vdots & \ddots & \vdots & \vdots \\ \mathbf{0} & \mathbf{0} & \mathbf{0} & \cdots & \Delta_{K-1} & \mathbf{0} \\ \mathbf{0} & \mathbf{0} & \mathbf{0} & \cdots & \mathbf{0} & \Delta_K \end{bmatrix} \begin{bmatrix} u_0(\cdot, t) \\ u_1(\cdot, t) \\ u_2(\cdot, t) \\ \vdots \\ u_K(\cdot, t) \end{bmatrix} \\
 &= \begin{bmatrix} \Delta_0 u_0(\cdot, t) \\ \Delta_1 u_1(\cdot, t) \\ \Delta_2 u_2(\cdot, t) \\ \vdots \\ \Delta_K u_K(\cdot, t) \end{bmatrix} = \begin{bmatrix} \frac{\partial_0 u(\cdot, t)}{\partial t} \\ \frac{\partial_1 u(\cdot, t)}{\partial t} \\ \frac{\partial_2 u(\cdot, t)}{\partial t} \\ \vdots \\ \frac{\partial_K u(\cdot, t)}{\partial t} \end{bmatrix}.
 \end{aligned}$$

Observe that each block Δ_k governs the diffusion process on the set of k -simplices. Since the matrix $\Delta_{\mathcal{G}}$ is block-diagonal, the heat equation $\frac{\partial u_{\mathcal{G}}}{\partial t} = -\Delta_{\mathcal{G}} u_{\mathcal{G}}$ decouples into $K+1$ separate equations, each corresponding to $\frac{\partial_k u(\cdot, t)}{\partial t} = -\Delta_k u_k(\cdot, t)$. Hence, the heat flow on the simplicial graph \mathcal{G} matches the heat flow across all orders in the original simplicial complex, provided the initial conditions on each order are consistent.

Therefore, the solution to the heat equation on the simplicial graph constructed by stacking $\Delta_0, \dots, \Delta_K$ agrees with the solution to the heat equation for each order of the simplicial complex when the initial conditions align. This justifies that the block-diagonal operator $\Delta_{\mathcal{G}}$ captures the same diffusion dynamics as the collection of separate operators acting on their respective simplices.

D. Theorem 4.4

Theorem D.1 (Capturing Geodesic Distance). *Let \mathcal{S} be a simplicial complex of order K , and let $\mathcal{G}(\mathcal{S})$ be its associated simplicial graph. Denote the heat kernel on \mathcal{S} by $H_t^k(\sigma, \tau)$, where σ, τ represent simplices of any order in \mathcal{S} . Assume that $H_t^k(\sigma, \tau)$ satisfies the heat equation:*

$$\frac{\partial H_t^k(\sigma, \tau)}{\partial t} = -\Delta_k H_t^k(\sigma, \tau), \tag{9}$$

where Δ_k is the k -Hodge laplacian. Then, by computing the heat kernel on the simplicial complex, we can accurately approximate the geodesic distance $d_{\mathcal{M}}(\sigma, \tau)$ on the manifold \mathcal{M} .

Proof. We have already shown that the heat equation on simplicial complexes \mathcal{S} agrees with the heat diffusion on the simplicial graph $\mathcal{G}(\mathcal{S})$. The heat kernel on the simplicial graph \mathcal{G} is given by:

$$H_t(\sigma, \tau) = e^{-t\Delta_{\mathcal{G}}}, \tag{10}$$

where $d(\sigma, \tau)$ represents the Euclidean distance between x and y .

From this expression, it follows that:

$$\begin{aligned}
 H_t &= e^{-t\Delta_{\mathcal{G}}} \\
 \log H_t &= \log e^{-t\Delta_{\mathcal{G}}} \\
 \log H_t &= -t\Delta_{\mathcal{G}} \\
 -4t \log H_t &= 4t^2 \Delta_{\mathcal{G}} \\
 -4t \log H_t(\sigma, \tau) &= 4t^2 \Delta_{\mathcal{G}}(\sigma, \tau)
 \end{aligned}$$

The operator Δ_G is constructed from distances between two simplices. Based on that, we can observe that,

$$\lim_{t \rightarrow 0} -4t \log h_t(\sigma, \tau) = d(\sigma, \tau)^2. \quad (11)$$

Varadhan (1967) shows that Eq 11 holds even for Riemannian manifolds with $d(\sigma, \tau)$ being the geodesic distance. Hence, we can approximate the geodesic distances using the diffusion on simplices. \square

E. Data Cohorts

- **Melanoma:** We use data originally collected by Ptacek et al. (2021) and published in Vesely & Johnson (2025), which consists of 54 melanoma patients, who underwent checkpoint blockade immunotherapy, each with approximately 489 to 1784 T-lymphocytes cells, resulting in a total of 11,862 cells. Each T-cell is characterized by 29 protein markers measured by Multiplexed Ion Beam Imaging (MIBI) (Yeo et al., 2024; Angelo et al., 2014). This data can be modeled as 54 point clouds in a 29-dimensional space, with sample sizes ranging from 489 to 1784 points per point cloud. The learning task is binary classification of whether the patient experienced recurrence or not (including stable disease as a ‘non-recurrence’), predicted from the protein expression levels. Note that we are not using the spatial resolution of MIBI in our use case.
- **Patient-derived Organoids (PDOs):** Third, we consider data from (Ramos Zapatero et al., 2023) featuring patient-derived organoids (PDOs) from 12 different patients with colorectal cancer. Patient-derived organoids (PDOs) are cell cultures grown from patient tumor samples. Each culture, representing a PDO sample, is characterized by 44 gene expression markers and contains approximately 1137 cells. Collectively, we consider 1,678 such cultures, forming 44 dimensional point clouds, resulting in a total of 2 million cells. The goal is to infer treatment administered to the PDO based on cellular states, serving as a synthetic task for our model.
- **Spatial Transcriptomics (ST):** We next consider Spatial Transcriptomics data generated using a 40-plex CODEX (CO-Detection by Indexing) immunofluorescent imaging workflow from (Wu et al., 2022), capturing 40 protein markers for each cell from 500 head-and-neck and colorectal cancer patients. Thus, each sample naturally splits into two views:
 - *Spatial View:* Cellular coordinates describing how cells are arranged in two-dimensional tissue sections.
 - *Gene View:* Dozens of markers or transcripts measured per cell, detailing complex biological states.

The overarching goal is to predict outcome of chemotherapy on cancer patients. Another goal is to predict cancer relapse of recovered patients. This task particularly leverages HiPoNet’s ability to fuse spatial context with transcriptional signals for clinically relevant insights in cancer research.

F. Experimental Setup

The parameters of HiPoNet are optimized using the AdamW optimizer (Loshchilov & Hutter, 2017) with a constant learning rate of 10^{-4} and a weight decay of 10^{-4} . We train the model for 20 epochs on every dataset for each model. We record the best metric (accuracy in classification tasks; mean squared error in regression tasks) achieved on the test set in each training run. We compare model performances on each dataset and task by the mean and standard deviation of their resulting five metric scores. For the spatial transcriptomics data, we use the folds from Wu et al. (2022). In Table 5, we describe order of the simplicial complex that we have used for each data set. Typically, our setup necessitates approximately two to three hours of training time for each dataset on a single NVIDIA A100 GPU.

F.1. Baselines

We compare the performance of HiPoNet on the classification tasks outlined in Section 5.2 to two groups of alternative methods. First, to demonstrate the expressive power of our multiview graph embeddings over traditional graph neural network techniques, we construct K-nearest neighbor graphs of the input point cloud data and attempt to learn a classifier using several popular graph neural network architectures. These include Graph Convolutional Networks (GCN) (Kipf & Welling, 2017), GraphSAGE (Hamilton et al., 2017), Graph Attention (GAT) Networks (Velickovic et al., 2018), Graph Isomorphism Networks (GIN) (Xu et al., 2019), and Graph Transformer Networks (GTNs) (Dwivedi & Bresson, 2020). We discuss their performance on our high-dimensional tasks in Section 5.

Data	Task	K
Melanoma-subsampled	Classification	2
	Persistence prediction	2
Melanoma-full	Classification	1
	Persistence prediction	1
PDO	Classification	1
	Persistence prediction	1
DFCI	Outcome	1
Charville	Outcome	2
	Recurrence	1
UPMC	Outcome	2
	Recurrence	1

Table 5. Order of simplicial complex

Num. of Views	Melanoma	PDO
1	27.27 ± 12.85	59.80 ± 1.99
2	<u>54.54 ± 11.13</u>	<u>61.10 ± 0.17</u>
4	90.90 ± 4.92	63.10 ± 0.00

Table 6. Accuracies (mean ± standard deviation) from ablation on the number of graphs. Best result is bolded and second best is underlined.

Second, we compare our method directly state-of-the art, bespoke point cloud learning methods. While DGCNN (Wang et al., 2019), PointNet++ (Qi et al., 2017b) and PointTransformer (Zhao et al., 2021) all perform very well on the three-dimensional problems they were designed to tackle, as we discuss below, they struggle to successfully classify high-dimensional point clouds.

G. Computational Complexity

The computational complexity of one step of diffusion process has the complexity of $\mathcal{O}(D(\sum_{k=1}^K N_k))$, where D is a dimension of the features. Since we have to repeat the diffusion process for a total of J times, and we have to calculate the wavelet co-efficients V times, the complexity calculating SWT is $\mathcal{O}(VJD(\sum_{k=1}^K N_k))$. The complexity of reweighing through hadamard product is $\mathcal{O}(DN_0)$. The complexity of VR-filtration is $\mathcal{O}N_0^2$. So, the total computational complexity of HiPoNet is $\mathcal{O}(N_0^2 + DN_0 + VJD(\sum_{k=1}^K N_k))$.

H. Additional experimental results

In Table 6, we present an ablation study of HiPoNet showing the impact of varying number of views. The results show that four views is most effective for capturing the topology of the point clouds.